

Comparison of Cephalic and Extracranial Montages for Transcranial Direct Current Stimulation – A Numerical Study

Gregory M. Noetscher, *Student Member, IEEE*, Janakinadh Yanamadala, Sergey N. Makarov, *Senior Member, IEEE* and Alvaro Pascual-Leone

Abstract—While studies have shown that the application of Transcranial Direct Current Stimulation (tDCS) has been beneficial in the stimulation of cortical activity and treatment of neurological disorders in humans, open questions remain regarding the placement of electrodes for optimal targeting of currents for a given functional area. Given the difficulty of obtaining in vivo measurements of current density, modeling of conventional and alternative electrode montages via the Finite Element Method (FEM) has been utilized to provide insight into tDCS montage performance. It has been shown that extracranial montages might create larger total current densities in deeper brain regions, specifically in white matter as compared to an equivalent cephalic montage. Extracranial montages might also create larger average vertical current densities in the primary motor cortex and in the somatosensory cortex. At the same time, the horizontal current density either remains approximately the same or decreases. The metrics used in this paper include either the total local current density through the entire brain volume or the average vertical current density as well as the average horizontal current density for every individual lobe/cortex.

Index Terms— In vivo current density, Transcranial direct current stimulation.

I. INTRODUCTION

TRANSCRANIAL DIRECT Current Stimulation (tDCS) has been used for the treatment of various neurological and

This work was submitted for review October 22nd, 2013

G. M. Noetscher is a PhD student in the Electrical and Computer Engineering department of the Worcester Polytechnic Institute, Worcester, MA 01605 USA (e-mail: gregm@wpi.edu)

J. Yanamadala is a PhD student in the Electrical and Computer Engineering department of the Worcester Polytechnic Institute, Worcester, MA 01605 USA (e-mail: jyanamadala@wpi.edu)

S. N. Makarov is a Professor of Electrical and Computer Engineering department at the Worcester Polytechnic Institute, Worcester, MA 01605 USA (e-mail: makarov@wpi.edu)

A. Pascual-Leone is the Director of the Berenson-Allen Center for Noninvasive Brain Stimulation at Beth Israel Deaconess Medical Center Boston, MA 02215 USA (e-mail: apalone@bidmc.harvard.edu)

Copyright (c) 2013 IEEE. Personal use of this material is permitted. However, permission to use this material for any other purposes must be obtained from the IEEE by sending an email to pubs-permissions@ieee.org.

psychiatric disorders, including depression, anxiety, and Parkinson's disease [1], [2]. Studies have shown that patients undergoing the procedure experience positive behavioral modifications with minimal negative effects that may include skin irritation, mild redness and itching under the electrode, headache, nausea, dizziness or a slight tingling sensation. Additionally, generation of toxins induced by an electrochemical reaction at the electrode-tissue interface are possible and application of tDCS above skull defects or inadequate electrode contact may produce focused current flow that has the potential to cause damage to skin and nerve tissue. Use of tDCS remains a very active area of research with the potential to non-invasively treat many of humanity's long standing disorders.

A number of electrode configurations, known as montages, are in use to control the application of current and concentrate the current density onto a particular area of the brain. These montages have been traditionally constructed based on knowledge of human anatomy and physiology. For example, if stimulation of the visual cortex is desired, an anode and cathode would be placed at the rear center and top center of the head, respectively. In this way, a particular area of the brain is identified for stimulation via tDCS and a montage that activates that area in a targeted manner is selected. One would assume that a large portion of the current leaving the anode would pass through the visual cortex while traveling to the cathode. In-vivo measurements have been reported [3] in the brain of a monkey and were used as the basis of constructing a model of the head that may be used to predict current flow in the brain from surface electrodes. However, real-time measurements and evaluation of individual anatomy remain challenges. To this end, extensive application of modeling and simulation techniques, including the Finite Element Method (FEM) have been used to characterize and understand the impacts of electrode arrangements on the human form, along with other factors including electrode size, the number of anode and cathode locations and current density [4-8]. The FEM has become such an important tool in the realm of tDCS that proposed general and customized, patient specific, and experimental tDCS protocols are examined and optimized using computational tools [9]. The models themselves have even acquired specific terminology and are known as 'forward models' with particular procedures on construction and usage

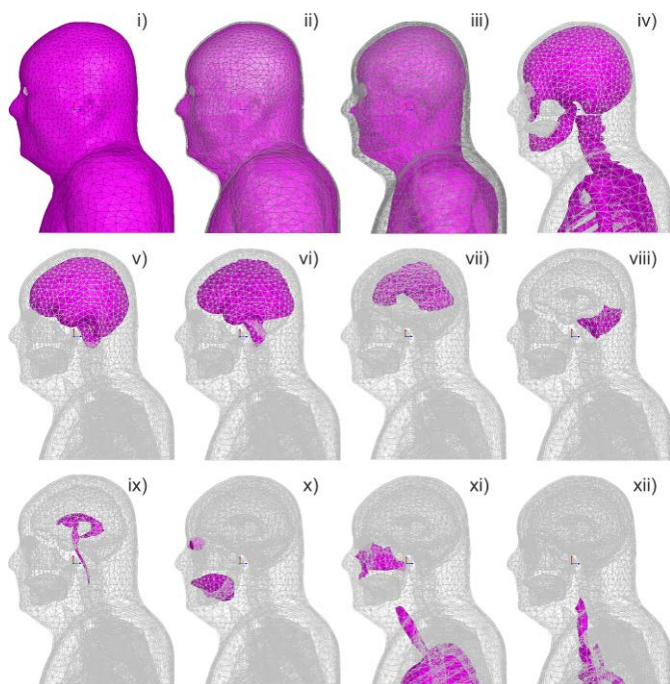


Fig. 1. Estimate for separate and distinct components of computational model employed for all tDCS simulations, each with individual material properties, including: i) – Artificial skin shell (2 mm thick); ii) – fat layer shell; iii) – muscle volume; iv) bones (left and right acromion, left and right humerus, jaw, ribs, left and right scapula, skull, spine), v) – closed CSF shell; vi) – cerebral cortex (grey matter); vii) – white matter; viii) – cerebellum; ix) – ventricles system; x) – eyes and tongue (separate tissues); xi) - sinus cavity, lungs and trachea; xii) – aorta and cava superior.

[10]. Clearly, the level of effort demonstrated in model construction and the prevalence of research based on modeling and simulation techniques indicates that conscientious use of FEM and other numerical method based solvers coupled together with anatomically accurate and predictive forward models [11] represents a realistic and efficient means that provides scientists, engineers and medical personnel detailed information on the performance of tDCS hardware in the very complex and multi-variant human body environment. Studies that take into account the effects of anisotropic conductivity in human tissues, including the skull and white matter, have demonstrated the importance of considering this physical condition when using forward models [12-13].

Despite existing studies and techniques that seek to manipulate the locality and depth of the stimulated area [14-17], open questions remain on the role of the cathode in terms of placement on the body. Field localization is strongly desired to provide tDCS practitioners the ability to treat certain disorders through precise targeting of specific areas or structures of the brain. Extracerebral locations (e.g., neck) of the cathode have been examined [18], along with the efficacy of a fronto-extracerebral montage in treatment of depression [19]. The impact of extracerebral montages on the brain stem and associated organs and tissues remains a concern [20], though the influence of these montages on cardio-vascular and autonomous functionality has been discussed in [21].

II. PROBLEM STATEMENT AND PAPER ORGANIZATION

The focus of this work is the simulation of the volumetric current density in the brain with electrodes configured in a

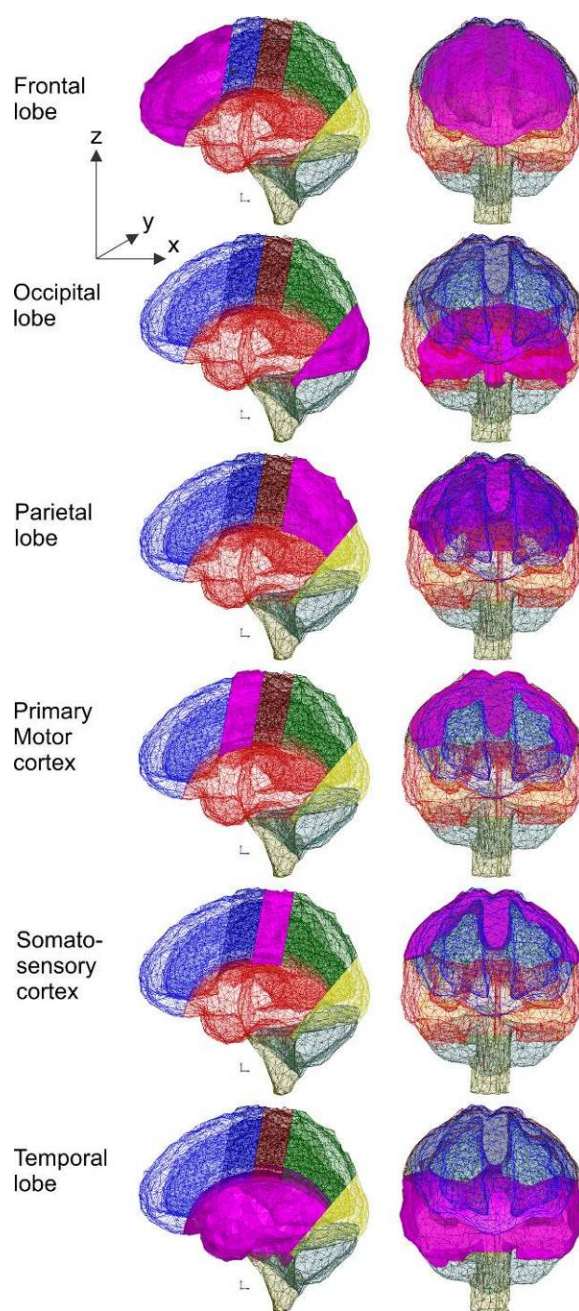


Fig. 2. Separation of the cerebral cortex into computational subregions including the frontal lobe, the occipital lobe, the parietal lobe, the primary motor cortex, the somatosensory cortex, and the temporal lobe.

cephalic (C3-Fp2) versus extracerebral manner with evaluations of cathode placement on both ipsi- and contralateral shoulder locations.

The FEM phantom used for this purpose is shown in Fig. 1 and thoroughly described in Section III. The anatomical brain segmentation included grey matter, white matter, ventricles, and cerebellum – see Fig. 1. The numerical simulation setup is described in Section IV. Electrode constitution and assembly is reported in Section V.

The cerebral cortex has been numerically defined as the Boolean difference between the grey matter and the white matter meshes. The cerebral cortex has further been artificially subdivided into individual lobes and cortices as shown in Fig. 2.

Section VI provides qualitative and quantitative results for the *local current density magnitude* within the brain volume. We visualize the total current density by plotting current on the surfaces of both the cerebral cortex and white matter. Alternatively, we visualize the total current density using a series of cut planes, each of which is accompanied by the corresponding cut plane atlas. Section VI also discusses the invariance of the *relative current density magnitudes* to significant changes in skin properties. We considered two extreme cases of wet and dry skin, respectively. Along with its primary goal, this study indirectly addresses the effect of changes in the contact between electrode and skin throughout the course of an extended tDCS treatment.

Section VII reports quantitative results for both the *average vertical current density magnitude* and the *average horizontal current density magnitude* in every individual lobe and/or cortex shown in Fig. 2 along with the global coordinate system employed. The corresponding current densities are defined by

$$J_z^{avg} = \frac{1}{V} \int_V |J_z(\mathbf{r})| d\mathbf{r},$$

$$J_{xy}^{avg} = \frac{1}{V} \int_V \sqrt{J_x^2(\mathbf{r}) + J_y^2(\mathbf{r})} d\mathbf{r}$$
(1)

where V is the volume of the tissue under study and $\mathbf{J}(\mathbf{r})$ is the spatial vector current density in this volume.

Section VIII estimates the expected electrode voltages and quantifies voltage responses due changes in properties of individual anatomical tissues.

Section IX also compares the results of the present paper with the previous numerical simulations.

Finally, Section X concludes the paper.

III. VHP-F MODEL AND SIMULATION DESCRIPTION

Construction of the forward model used in this study was enabled by the processes of medical image data acquisition, manual segmentation, mesh conditioning, and model registration. All surfaces describing a particular geometry must be 2D manifold and possess a sufficiently high triangle quality, as element quality has been proven to be vital to the accuracy of the simulation [22].

A. Data Acquisition

The model utilized in this study was constructed using anatomical cryosection images of the axial plane provided by the Visible Human Project[®] (VHP) established in 1989 by the U.S. National Library of Medicine (NLM) [23]. Male and female data sets became available in November of 1994 and 1995, respectively. Each consisted of MRI, CT and cryosection images taken predominantly in the axial plane of the bodies of various resolutions. Anatomical cryosection image data from the female patient, consisting of 2048 by 1216 pixels with each pixel measuring 0.33mm per side, was used exclusively in the construction of the model for the present study, producing the VHP-F nomenclature [24]. The original VHP-NLM model resolution in the axial plane is limited by image pixel density, and if we assume the segmentation is legitimate and accurate, produces a resolution value of 0.33mm by 0.33mm. Since every third image in the

dataset was utilized, resolution along the vertical axis of the body is limited to 0.99mm. A voxel produced by images used in this manner would have x-, y-, and z-dimensions of 0.33mm by 0.33mm by 0.99mm.

B. Segmentation

Image segmentation is an area of active research with many dynamic and varying methodologies [25-34]. Despite this diversity in implementation, no one singular technique has proven to be suitable in all applications or as accurate as manual segmentation by a human operator. Though extremely time consuming, it is for this reason that manual segmentation was employed almost exclusively for the development of the models used in this study.

One of the major tools included in the development of the VHP was the open source program Insight Toolkit (ITK), which enables the analysis of three dimensional image stacks and simultaneous segmentation of images in the axial, coronal, and sagittal body planes via manual and automatic methods [35]. Image stacks are read into ITK for segmentation and the user may manually trace organs, tissues and other structures, thus isolating these regions from other image areas. The end result is a stereolithography (STL) file describing the surface of the segmented region as a series of dense triangular elements (surface Delaunay triangulation) defined by a node point cloud.

C. Mesh Conditioning and Registration

The results of the segmentation process are very fine and dense meshes that contain a large number of nodes. Typical numbers of nodes are on the order of between 10^6 and 10^{10} . These meshes, while accurate with respect to the image

TABLE I
ELECTRICAL PROPERTIES EMPLOYED DURING SIMULATION [46]

Structure	FEM Material	Conductivity (S/m)
Sinus Cavity	Air	0
Aorta	Blood	0.7
Superior Vena Cava		
Acromion	Homogeneous Bone (a combination of cancellous/cortical types)	0.0756/0.02
Humerus		
Jaw		
Ribs		
Scapula		
Skull		
Spine		
Gray matter	Brain	0.0275
White Matter	Brain	0.0277
Cerebellum	Cerebellum	0.0475
Cerebrospinal Fluid (CSF)	CSF	2
Ventricle system		
Eye	Vitreous Humor	1.5
Fat Layer	Fat	0.0377
Lung	Inflated Lungs	0.0389
Trachea		
Muscle Layer	Muscle	0.202
Skin Layer	Dry Skin	0.0002
Tongue	Tongue	0.8

dataset, would be too unwieldy to be used in an FEM simulation. Mesh conditioning is required to reduce the number of nodes to a computationally reasonable number and ‘clean’ the mesh, eliminating defects and discrepancies that could reduce the accuracy and utility of the model.

Much of the mesh conditioning process has been accomplished via MeshLab [36]. Example operations include selective reduction of the number of nodes via Quadric Edge Collapse Decimation [37] which was accomplished to remove elements in areas of relatively coarse features (e.g., top of the chest) while retaining elements in regions that require finer detail. Relative triangle sizes in those areas may vary by as much as 1:5 while keeping a reasonably high triangle quality everywhere. Smoothing functions were achieved using HC Laplacian Smoothing [38] in order to retain the original shape volume. Additional defects, including redundant nodes and edges, non-manifold edges, and intersecting faces can be eliminated via Delaunay triangulation [39]. In certain cases, rebuilding the mesh by Poisson Surface Reconstruction [40] has proven to eliminate element folding and produce smooth and contiguous surfaces suitable for simulation purposes.

Following the segmentation and conditioning processes, all individual components of the VHP-F model were registered to ensure proper position, size and shape. Registration was accomplished by overlaying the digitized structures over the original cryosection images and any required adjustments were made on a node by node or element by element basis. In this way, any distortions, rotations or imperfections created by the operations mentioned above were addressed.

IV. SIMULATION SETUP

The results of the mesh generation process described above can be seen in Figs. 1-2. Each structure was converted to the NASTRAN file format to facilitate importation into commercial numerical solvers. Final assembly of all components that make up the model required verification that no structures were overlapping or intersecting. Additionally, each structure required assignment of appropriate material properties.

A. Material Properties

Electromagnetic modeling of the human body requires meticulous and cautious definition of the associated material properties resident within the simulation. A wealth of research on the subject is available [41-46] demonstrating the variability of values across multiple types of tissues and a high dependence on frequency. For low frequency and static simulations such as the ones described in this work, material conductivity is paramount. A summary of tissue types and conductivity values is given in Table I [46].

B. FEM Software and Numerical Accuracy

Static electromagnetic simulations were conducted using ANSYS’ Maxwell 3D version 16 product. This software numerically obtains a unique solution to Maxwell’s equations at DC via the FEM and user specified boundary conditions. The Maxwell product has extensive mesh analysis and healing capabilities. Most important, solution convergence and the ultimate accuracy is controlled through a rigorous adaptive mesh refinement procedure. For the results presented below,

five iterations of adaptive mesh refinement were employed, each with a refinement level of 30% per pass. This process grew the total number of tetrahedral elements from approximately 200,000 to over 600,000 with total runtimes on the order of about six hours on a server with 192 Gbytes of RAM. When solving a DC current conduction problem, the Degrees of Freedom (DoF) are the electric scalar potentials at each node of the tetrahedral mesh. Typical values of mesh size per iteration and energy loss are given in Table II and demonstrate a reduction of the residual error through successive refinement steps, increasing the accuracy of the calculation as it converges.

C. Boundary Conditions and Excitations

The default boundary conditions used by ANSYS MAXWELL 3D during DC conduction type simulations are as follows. Standard (or “natural”) boundaries are enforced at inner object interfaces and ensure the continuity of the normal component of the direct electric current density through the interfaces. Homogeneous Neumann boundaries imposed on all outer boundaries do not allow the normal electric current to pass. The electric field within the conductor is indeed tangential on this outer boundary. We have found that MAXWELL 3D does not implement an ideal hypothetical current source with a fixed current density and a variable voltage across the electrode surface. Instead, a more realistic voltage source model with Dirichlet boundary conditions of a fixed surface electrode voltage is internally used for both voltage and current excitations. After completing the simulations, the required total current may be related to voltage. A user can define the total current a priori, which is the current source implementation. The well-known current singularity at the voltage electrode edges is eliminated via matching sponges – see the next Section.

TABLE II
CONVERGENCE OF A TYPICAL CASE BASED ON TETRAHEDRAL MESH SIZE

Adaptive Pass	Number of Tetrahedra	Total Loss (mW)	Loss Error (%)	Delta Loss (%)
1	183,113	0.6	1.10	N/A
2	248,020	0.607	0.33	1.17
3	335,946	0.60915	0.19	0.35
4	455,431	0.61047	0.13	0.22
5	616,856	0.61137	0.09	0.15

V. ELECTRODES AND THEIR MONTAGES

A. Electrode Model

Electrodes were simulated using rectangular blocks of material (sponges) with the conductivity of saline solution (2 S/m). Electrodes were sized consistent with existing procedures and protocols [1] such that the rectangular surface in conformal contact with the skin was 5 cm on a size with a total surface area of 25 cm². Each electrode was constructed in a virtual environment by subtracting larger geometric blocks that intersected the surface of the VHP model with the skin of the model. In this way, the contacting surface of the electrode was made conformal such that, even in areas of high curvature

on the model, full contact was maintained and no space existed between the electrode and the skin. A total electrode current of 2 mA (with the equivalent uniform density of $0.08\text{mA}/\text{cm}^2$ [1]) was employed as the source in all cases described below.

B. Electrode Montages

Electrodes were arranged in three different configurations: following the Modified Combinatorial Nomenclature (MCN) of the International EEG 10-20 system, we simulate the C3-Fp2 montage, which has been traditionally used to stimulate the primary motor cortex (M1) by placing the stimulation electrode at the top-left portion of the head and the reference electrode at the contralateral supraorbital position; an extracephalic contralateral shoulder montage which retains the original excitation electrode position but shifts the reference electrode to the opposite side shoulder; and extracephalic ipsilateral shoulder montage which also retains the original excitation electrode position but shifts the reference electrode to the shoulder on the same side of the body as the excitation. Electrode positions and a cut plane atlas may be viewed in the upper 2 rows of Figs. 4-8. The cut plane atlases show that the layer of muscle around the head is essentially non-existent (see Figs. 4-6) and only contributes to the model at regions midway and below the skull – see Figs. 7 and 8. Skin and fat layers mostly contribute to conduction around the head.

VI. SIMULATION RESULTS FOR TOTAL CURRENT DENSITY

A. Total Current Density for Surfaces of Cerebral Cortex and White Matter

The total current density magnitude is plotted on the surfaces of the cerebral cortex and white matter in rows 2 and 3 of Fig. 3, respectively. The traditional cephalic montage in column 1 demonstrates a significant amount of current at the anterior of the grey matter as it passes to the supraorbitally located cathode. The surface plots of the extracephalic configurations exhibit much lower current densities in this region of the brain with higher concentrations toward the posterior.

When stimulated with an extracephalic configuration, the current on the surface of the white matter appears to be slightly more concentrated directly below the anode, suggesting a relatively deeper penetration with less current passing through the anterior of the frontal lobe.

B. Total Current Density for Sagittal Cut Planes

A series of plots portraying the current densities experienced with each montage are presented in Figs. 4-8 and all figures are displayed with the same scale for comparison purposes. Figs. 4-6 (similar to Fig. 3) are divided into columns i – iii which depict current density results from the traditional, contralateral and ipsilateral shoulder montages projected onto a sequence of sagittal dissecting planes that progressively shift from the anode through the head and towards the right side of the model. In all cases, the shunting nature of the high conductivity Cerebrospinal Fluid (CSF) is quite apparent as high proportions of the total current are seen passing through this layer surrounding the brain. This characteristic is plainly seen on the third rows of Figs. 4-6, which provide images of the brain that include the surrounding structures. The high

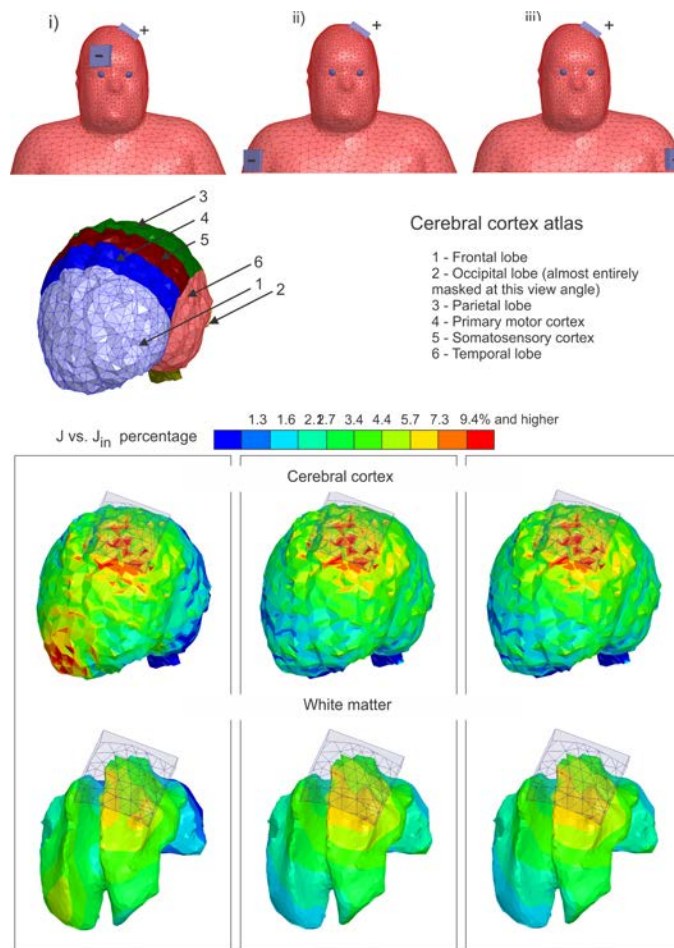


Fig. 3. Surface plots of the total current density on the cerebral cortex (row 2) and white matter (row 3). Total current density normalized by the input current density at the electrodes is shown. Column 1 provides results for the cephalic configuration while columns 2 and 3 display the contra-lateral and ipsi-lateral extracephalic results, respectively, using a logarithmic scale.

amount of current shown in the third row of Fig. 5 is due to the presence of the ventricle system at the center of the head.

A sagittal plane passing through the anode is depicted in Fig. 4. Relatively higher proportions of the current are observed in the primary motor cortex of the extracephalic cases. Additionally, the depth of stimulation appears relatively greater in both extracephalic configurations.

A second sagittal plane located at the approximate midpoint between the anode and the contralateral supraorbital cathode position is shown in Fig. 5. The current levels within the brain depicted in this plane provide evidence that the higher levels of current are present in the frontal lobe in the cephalic arrangement. Both extracephalic arrangements again indicate a slightly deeper level of stimulation. Current density values in Fig. 5 indicate that there is some minor stimulation of the brain stem when using extracephalic anode locations versus essentially no stimulation when using the traditional montage with the ipsilateral shoulder arrangement performing marginally better than the contralateral design. While current is present in the brain stem, the values are low and approximately 5 times less than current values in the area of desired stimulation.

A final sagittal plane passing through the contralateral supraorbital cathode position is presented in Fig. 6. Again, the

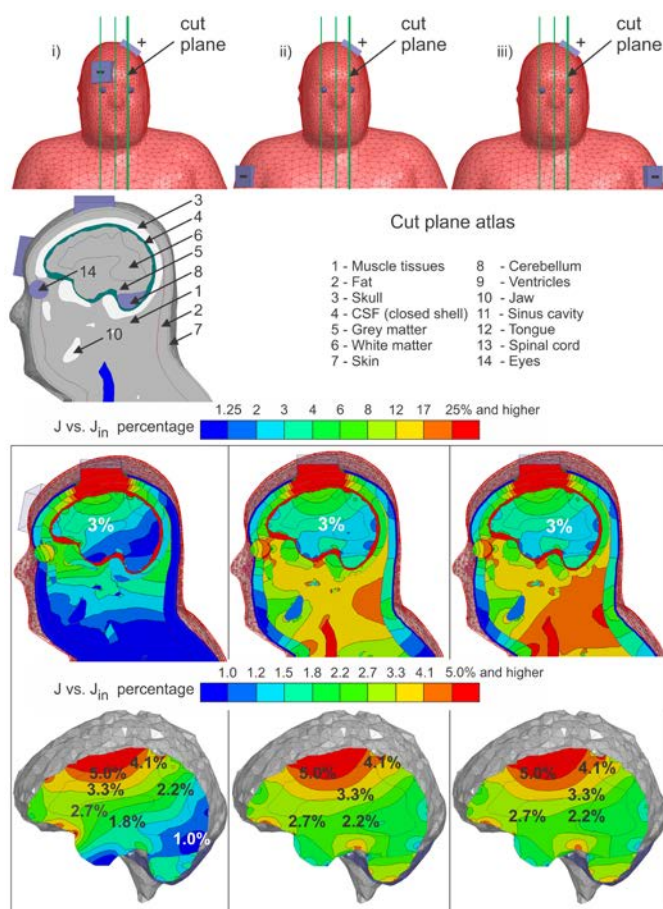


Fig. 4. Depictions of the contralateral supraorbital (i), extracephalic contralateral shoulder (ii), and extracephalic ipsilateral shoulder (iii) cathode montages. Total current density normalized by the input current density at the electrodes is shown projected onto three sagittal planes that progressively travel from left to right on the model using a logarithmic scale.

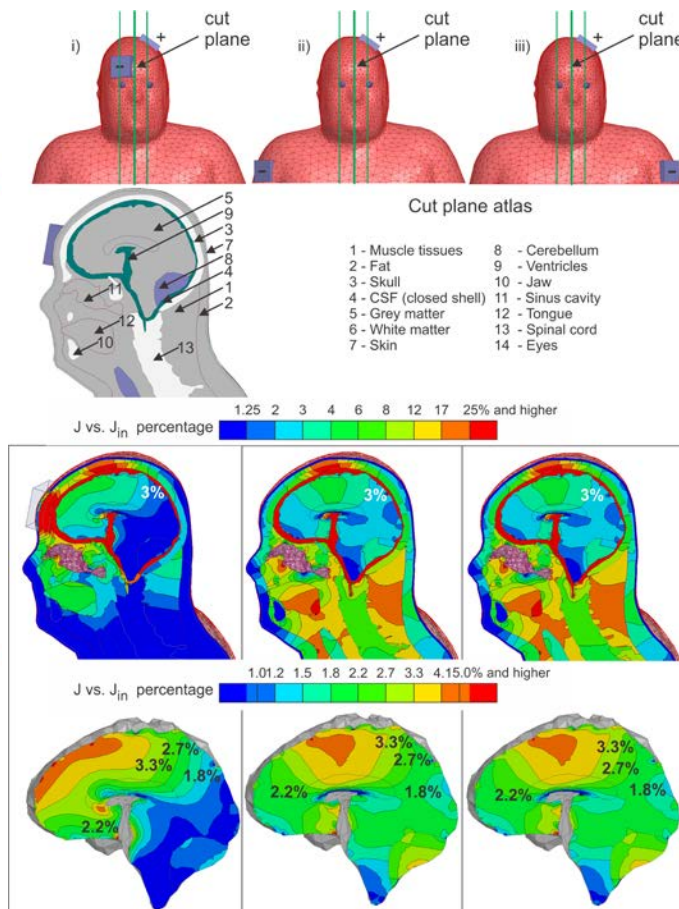


Fig. 5. Contralateral supraorbital (i), extracephalic contralateral shoulder (ii), and extracephalic ipsilateral shoulder (iii) cathode montages. Total current density normalized by the input current density at the electrodes is shown with surrounding body structures using a logarithmic scale.

cephalic configuration depicts a relatively larger percentage of the current passing through the prefrontal lobe as it moves toward the cathode. This would suggest stimulation of this region of the brain, which has been associated with planning and consciousness rather than body movement and coordination.

Special consideration should be given to the extracephalic configurations shown in Fig. 4-5. The depth of stimulation when using extracephalic cathode locations is visibly greater than that of the traditional cephalic arrangement. This would indicate that a greater percentage of the brain volume would be covered through extracephalic means.

This last observation about stimulation depth raises an interesting question of why electrodes placed in close proximity to what is essentially a highly conductive sphere of CSF encompassing the brain perform less efficiently than electrodes placed at farther locations.

C. Total Current Density for Axial Cut Planes

Fig. 7 depicts an axial plane located approximately midway through the brain and intersects with the supraorbital cathode location. Results displayed in this plane indicate relatively deep stimulation regions for both extracephalic designs as compared with the traditional montage. Conversely, the traditional electrode configuration shows a much higher level of current flowing into the cathode.

TABLE III
ELECTRODE VOLTAGES AND DIMENSIONLESS VOLTAGE RESPONSES. ALL DIMENSIONAL VOLTAGE DATA ARE RELATED TO A CURRENT SOURCE WITH THE ELECTRODE NORMAL CURRENT DENSITY OF $J_{in} = 0.08 \text{ mA/cm}^2$ AND THE TOTAL SOURCE CURRENT OF $I_m = 25 \text{ cm}^2 \times J_{in} = 2 \text{ mA}$

Parameter	Tissue					Brain (GM, WM, Cer)
	Skin	Fat	Muscle	Skull	CSF	
Conductivity	0.0002	0.038	0.2	0.076	2.00	0.028 0.028 0.048
C3-Fp2 Montage						
V_0 , mV	19.334					
V for 20% cond. change, mV	16.19	19.29	19.33	19.32	19.32	19.33
$S \times 10^3$	813	11	0	5	3	1
C3-Extracephalic Ipsilateral Shoulder Montage						
V_0 , mV	21.99					
V for 20% cond. change, mV	18.46	21.91	21.94	21.98	21.98	21.98
$S \times 10^3$	802	17	10	2	3	0
C3-Extracephalic Contralateral Shoulder Montage						
V_0 , mV	21.84					
V for 20% cond. change, mV	18.41	21.84	21.88	21.91	21.91	21.92
$S \times 10^3$	801	18	9	2	2	0

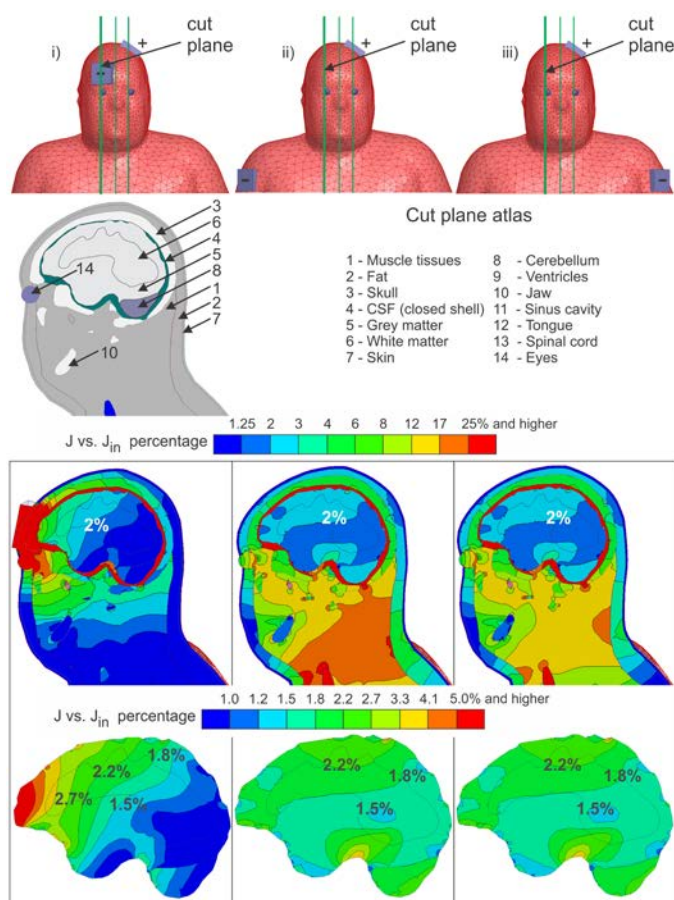


Fig. 6. Contralateral supraorbital (i), extracephalic contralateral shoulder (ii), and extracephalic ipsilateral shoulder (iii) cathode montages. Total current density normalized by the input current density at the electrodes is shown with surrounding body structures using a logarithmic scale.

D. Total Current Density for 45 Degree Cut Planes

A diagonal cut-plane traversing the space between the anode at the top of the head and the traditional location for the cathode is shown in Fig. 8. A cephalic cathode configuration seems to show a relative shift in current density from the motor cortex to the frontal lobe. Virtually no stimulation beyond the parietal lobe is seen and while extracephalic configurations seem to somewhat better target the motor cortex, some stimulation of the rear of the brain is evident. This behavior is consistent in previous figures.

E. Invariance of Relative Current Densities to Changes in Skin Properties

Relatively higher total current densities in the brain for extracephalic montages may be observed in Figs. 3-8. And yet, one potentially critical configuration would correspond to a very highly-conducting skin layer so that the bulk of current might be expected to flow closer to the surface, irrespective of the particular electrode montage (cephalic or extracephalic). As a test case, we consider here a hypothetical isotropic skin layer with the extreme conductivity of 0.25 S/m (wet epidermis) compared with dry skin from Table I in Fig. 9, which would model the electrode/skin interface as the electrode dries during an extended tDCS treatment session. Despite the expected overall decrease of the absolute current density in the brain, the relative patterns of current density

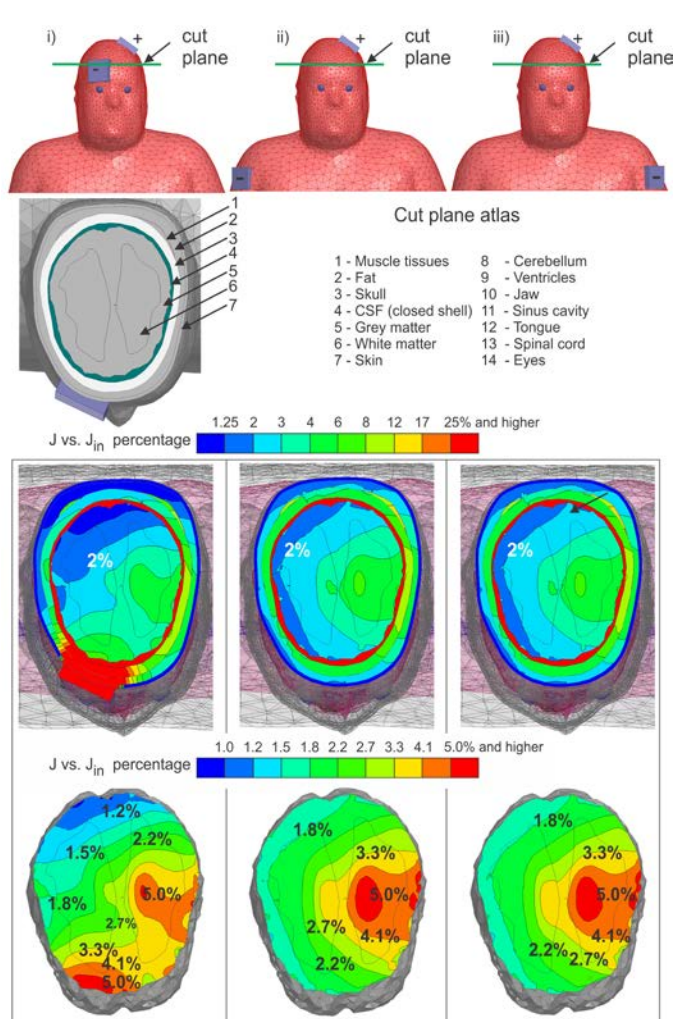


Fig. 7. Current densities projected onto an axial plane located halfway down the brain for the contralateral supraorbital (i), extracephalic contralateral shoulder (ii), and extracephalic ipsilateral shoulder (iii) montages. Total current density normalized by the input current density at the electrodes is shown using a logarithmic scale.

distribution remain approximately the same for all three tested montages shown in Fig. 9! We think that these results may be directly extrapolated to the anisotropic case. Another justification of this result will be discussed further with reference to Fig. 10.

VII. QUANTITATIVE EVALUATION OF VERTICAL AND HORIZONTAL AVERAGE CURRENT DENSITIES

Results presented thus far rely upon a visual inspection of the total current density distribution in the different observation planes or on surfaces. It may be useful to separate the total current density into two partial components (vertical and horizontal), and then find the average values of these components, J_z^{avg} , J_{xy}^{avg} for every lobe/cortex following Eq.

(1). Fig. 10 reports numerically found average vertical and horizontal components of current densities in the brain including its individual subregions defined in Fig. 2. It can be seen from Fig. 10a that the vertical component of current density in every subregion increases when extracephalic montages (the results for both of them are nearly identical and cannot be distinguished in the figure) are used. However, the

horizontal component of current density in Fig. 10b either decreases or remains nearly the same compared to the cephalic case. This may be instrumental when stimulating brain regions with cell structures that are biased in either the vertical or horizontal directions. The results for extremely wet skin shown in Fig. 10c, d, respectively, follow a similar tendency although the vertical current components in the primary motor cortex and in the somatosensory cortex become close to each other for both competing montages. Note that the cephalic montage is much less sensitive to variations in skin properties.

VIII. EXPECTED ELECTRODE VOLTAGES AND THEIR VARIATIONS

Cephalic and extracephalic configurations require different electrode voltages for the same amount of current. This section provides the corresponding estimates including voltage variation margins. To investigate this and related problems we introduce the voltage response of a tissue/organ to small changes in tissue conductivity. Given the independent current source I_{in} as an excitation, the dimensionless (dynamic or small-signal) voltage response may be defined as

$$S = -\frac{dV/V_0}{d\sigma/\sigma_0} > 0 \quad (2)$$

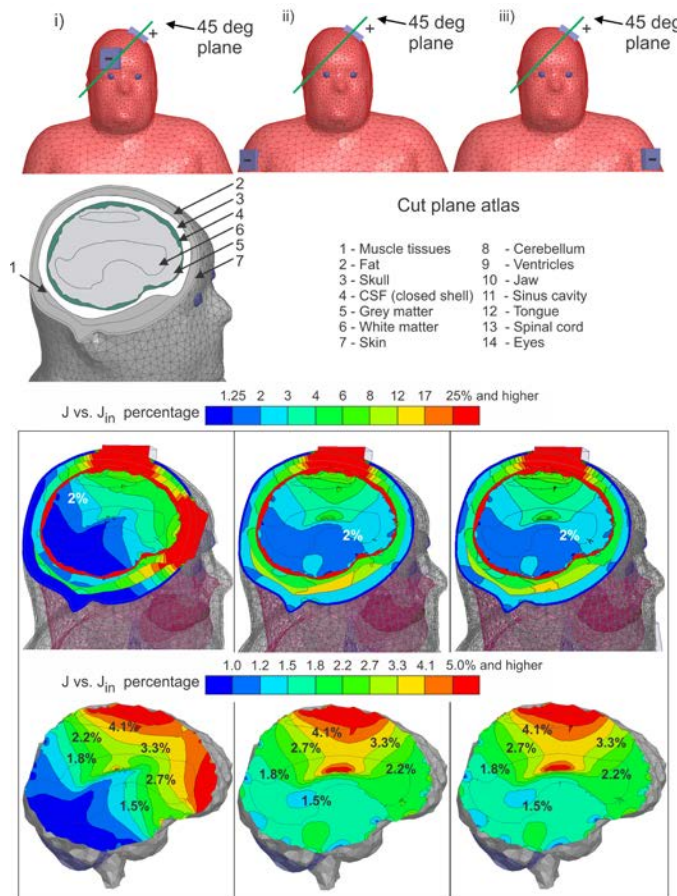


Fig. 8. Diagonal cut-plane between the anode and supraorbital cathode displaying normalized total current densities for the contralateral supraorbital (i), extracephalic contralateral shoulder (ii), and extracephalic ipsilateral (iii) montages using a logarithmic scale.

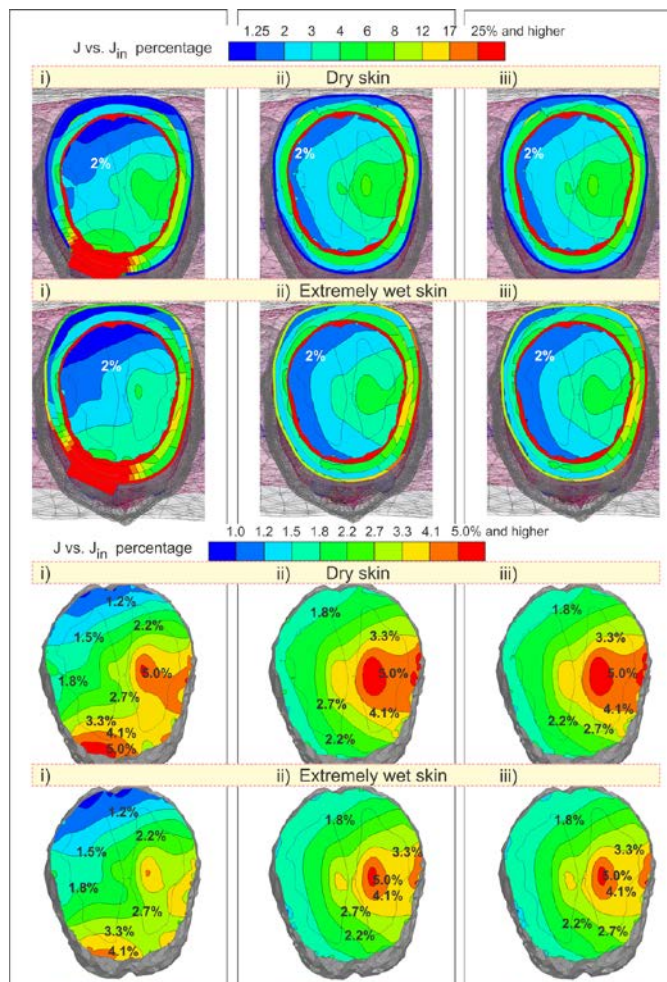


Fig. 9. Comparison of tDCS simulation results from Fig. 5 as a function of skin conductivity. Total current densities projected onto an axial plane located halfway down the brain for the contralateral supraorbital (i), extracephalic contralateral shoulder (ii), and extracephalic ipsilateral (iii) montages. Note that the images are employing a logarithmic scale.

where $d\sigma$ is the tissue conductivity variation and dV is the corresponding electrode voltage variation about the unperturbed state V_0, σ_0 . If a particular tissue carries a significant current, its corresponding voltage response should be large. This fact follows from the local form of Ohm's law. Table III summarizes unperturbed electrode voltages and voltage responses of individual tissues for the three electrode configurations. The C3-Fp2 montage possesses a very small voltage response for the muscle tissue since there is virtually no such tissue within the main current path (only the skin, and the fat are two layers around the skull). In this analysis, we consider the brain as one entity. Based on the results of Table III for individual voltage responses, we estimate the electrode voltages and their extremes given maximum $\pm 20\%$ conductivity variations for various montages as: (i) cephalic: $\sim 300 \text{ mV} \pm 60 \text{ mV}$; (ii) extracephalic ipsilateral: $\sim 720 \text{ mV} \pm 120 \text{ mV}$; (iii) extracephalic contralateral: $\sim 710 \text{ mV} \pm 120 \text{ mV}$.

IX. DISCUSSION

A. General Observations

Given the results described in the previous sections, the following observations can be made:

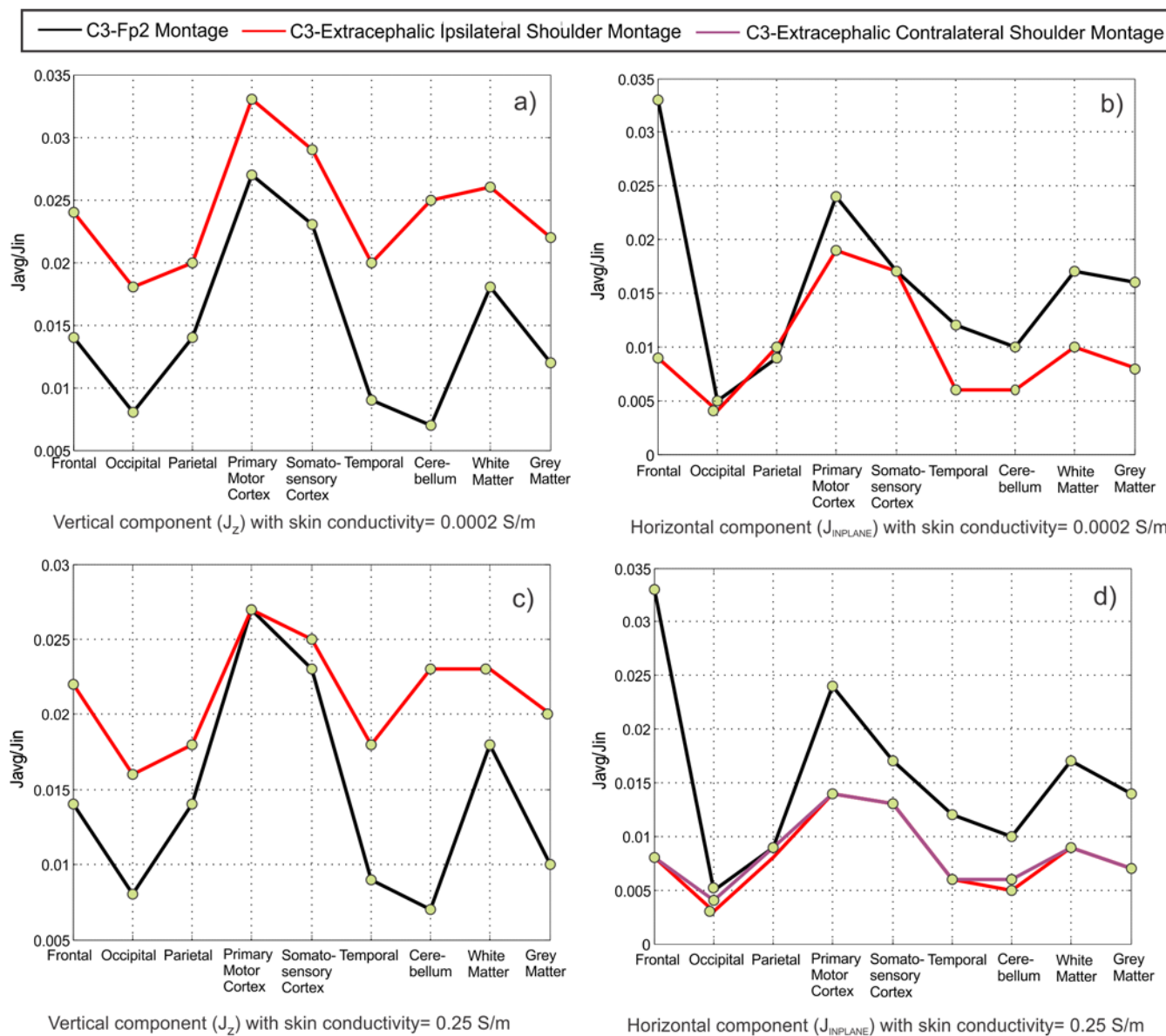


Fig. 10. Averaged values of the vertical and horizontal current density components for the brain substructures shown in Fig. 2 and total white and grey matter. Rows 1 and 2 depict results for dry and wet skin, respectively. Ipsi- and contralateral results were identical except in the lower right of Fig. 10d.

- I. Extracerephalic montages might create larger total current densities in deeper brain regions, specifically in white matter as compared to an otherwise equivalent cephalic montage.
- II. Extracerephalic montages might create larger average vertical current densities in the primary motor cortex and in the somatosensory cortex. At the same time, the horizontal current density either remains approximately the same or decreases.
- III. The previous observation becomes significantly less apparent for a very wet skin.
- IV. The extracerephalic montages may reduce the large percentage of the applied current passing through the frontal cortex when the cathode is located at the contralateral supraorbital location.

Indeed, the data presented in Figs. 3 through 10 is related to only one particular cephalic electrode configuration studied in

this paper. Furthermore, it is clearly dependent on both the model construction and tissue conductivity values.

To address the last concern, we have compared our findings with simulation data from a similar problem (cephalic versus extracerephalic configurations) solved numerically in Ref. [47]. The FEM model used in this work did not include any layer of fat (which has a significantly lower conductivity value [46]) around the skull. Instead, a homogeneous thick skin layer with a high conductivity value of 0.43 S/m has been used. The authors stated that “the use of extracerephalic montage does not significantly increase the amount of current penetration through the skull.” The figure of merit was apparently the current density map at the surface of the cerebral cortex. Such a result is in agreement with our data presented in Fig. 10c, d where we see that some potential advantages of the extracerephalic configuration may rapidly disappear when the skin conductivity becomes very high.

B. Invariance of Extracerephalic Montages

The density of current flow within the body during extracephalic stimulation is weakly dependent on the choice of the shoulder location. In both ipsi- and contralateral cathode montages, current densities in the human head are nearly identical. This makes intuitive sense, as current needs to flow toward the cathode through the neck. Above the neck, the current distribution is insensitive to shoulder electrode positions. This is similar to water flow in a closed container in the form of a human body where the anode is a source, the cathode is a sink, and the neck is acting as a choke point. Thus, there is freedom in choosing the extracephalic electrode location. This may alleviate concerns regarding extraneous stimulation of other body areas (i.e., disrupting the autonomic nature of heart muscle regulation by the sinoatrial node, etc.).

C. Validation of Results Across Configurations

Along with the previously reported extreme case, the current density distribution behavior observed in Figs. 3-10 has been confirmed for:

- i. Different tissue conductivities (every value was separately varied by $\pm 20\%$);
- ii. Different body mass values (scaling the entire structure by $5 \times 5 \times 5\%$ while keeping the electrode size the same);
- iii. Homogeneous versus non-homogeneous brain structures (assigning average conductivity values to white/grey matter/cerebellum).

D. VHP-F Model Limitations and Extensions

While the present VHP-F model has proven to be useful for numerical studies such as the one described in this work, it does have its limitations. In particular, the CSF flow present in the subarachnoid space is greatly simplified: only the thin yet non-uniform closed CSF shell and the ventricles are considered, as shown in Figs. 4-9. The minimum thickness of this shell was artificially set to 1 mm in order to avoid numerically inaccurate results. The skull is modeled by a homogeneous bone structure. All present calculations use lower-definition meshes with the typical resolution (surface deviation) ranging from 1mm to 3 mm, which significantly suppresses the fine sulci and gyri structures. Also, the brain membranes, including the pia mater, arachnoid, and dura mater, are not explicitly included in the VHP-F model. These membranes present a direct layer between the brain and stimulating electrodes and likely should be characterized for enhanced tDCS simulation accuracy. The balloon representation of the skin with the fixed uniform skin shell thickness of 2mm is indeed another simplifying approximation. However, the variable (and typically much thicker) fat layer of a greater conductivity just beneath the skin is anatomically correct to within 1 mm segmentation accuracy, everywhere in the phantom. Together, the skin and fat layers may still form a reasonable modeling approximation for the surface current flow. The impact of anisotropic materials on the performance of the VHP-F model is another item we wish to consider in a future work. Our host FEM software (MAXWELL 3D of ANSYS) allows for a diagonal Cartesian conductivity tensor $\sigma_{xx}, \sigma_{yy}, \sigma_{zz}$ though every tissue.

X. CONCLUSIONS

It has been shown that extracephalic montages might create larger total current densities in deeper brain regions, specifically in white matter as compared to an equivalent cephalic montage. Extracephalic montages might also create larger average vertical current densities in the primary motor cortex and in the somatosensory cortex. At the same time, the horizontal current density either remains approximately the same or decreases. The metrics used in this paper include either the total local current density through the entire brain volume or the average vertical and horizontal current densities for each individual lobe/cortex.

ACKNOWLEDGEMENTS

The authors wish to thank Dr. Mikhail Kozlov of the Max Planck Institute for Human Cognitive and Brain Sciences, Dresden, Germany for his feedback regarding human anatomy and model applicability and for his testing of the model when simulating Magnetic Resonance Imaging hardware. The authors are also very thankful to Dr. Sara Louie of ANSYS and Dr. Alexander Prokop of Computer Simulation Technology for their comprehensive testing of the VHP model and feedback regarding the model utility. Ms. Saili Maliye of Worcester Polytechnic Institute has also been instrumental in providing valuable contributions. We are very thankful to two anonymous reviewers for useful, very comprehensive, and inspiring comments and suggestions, which significantly improved the manuscript.

REFERENCES

- [1] M.A. Nitsche, L.G. Cohen, E.M. Wassermann, A. Priori, N. Lang, A. Antal, W. Paulus, F. Hummel, P.S. Boggio, F. Fregni, A. Pascual-Leone, "Transcranial Direct Current Stimulation: State of the Art 2008", *Brain Stimulation*, vol. 1, pp. 206-223, 2008.
- [2] A.R. Brunoni, M.A. Nitsche, N. Bolognini, M. Bikson, T. Wagner, L. Merabet, D.J. Edwards, A. Valero-Cabre, A. Rotenberg, A. Pascual-Leone, R. Ferrucci, A. Priori, P.S. Boggio, F. Fregni, "Clinical research with transcranial direct current stimulation (tDCS): Challenges and future directions", *Brain Stimulation*, vol. 5, pp. 175-195, 2012.
- [3] S. Rush, D.A. Driscoll, "Current distribution in the brain from surface electrodes", *Anaesth Analg Curr Res*, vol. 47, pp. 717-723, 1968.
- [4] M. Bikson, A. Rahman, A. Datta, "Computational models of transcranial direct current stimulation", *Clinical EEG and Neuroscience*, vol 43, pp. 176-183, 2012.
- [5] T. Wagner, F. Fregni, S. Fecteau, A. Grodzinsky, M. Zahn, A. Pascual-Leone, "Transcranial direct current stimulation: a computer-based human model study", *NeuroImage*, vol. 35, pp. 1113-1124, 2007.
- [6] A. Datta, M. Elwassif, F. Battaglia, M. Bikson, "Transcranial current stimulation focality using disc and ring electrode configurations: FEM analysis", *J. Neural Eng.*, vol. 5, pp. 163-174, 2008.
- [7] P.C. Miranda, M. Lomarev, M. Hallett, "Modeling the current distribution during transcranial direct current stimulation", *Clinical Neurophysiology*, vol. 117, pp. 1623-1629, 2006.
- [8] P.C. Miranda, A. Mekonnen, R. Salvador, G. Ruffini, "The electric field in the cortex during transcranial current stimulation", *NeuroImage*, vol. 70, pp. 48-58, 2013.
- [9] M. Bikson, A. Rahman, A. Datta, F. Fregni, L. Merabet, "High-resolution modeling assisted design of customized and individualized transcranial direct current stimulation protocols", *NeuroModulation: Technology at the Neural Interface*, vol. 15, pp. 306-315, 2012.
- [10] M. Bikson, A. Datta, "Guidelines for precise and accurate computational models of tDCS", *Brain Stimulation*, vol. 5, pp. 430-434, 2012
- [11] A. Datta, X. Zhou, Y. Su, L.C. Parra, M. Bikson, "Validation of finite element model of transcranial electrical stimulation using scalp potentials: implications for clinical dose", *J Neural Engineering*, vol. 10, pp. 2013.

